Title
Multiscale computational modeling of the effects of 2’-deoxy-ATP on cardiac muscle calcium handling

Journal
Journal of Applied Physics, 134(7)

ISSN
0021-8979

Authors
Hock, Marcus T
Teitgen, Abigail E
McCabe, Kimberly J
et al.

Publication Date
2023-08-21

DOI
10.1063/5.0157935

Peer reviewed

Journal of Applied Physics ARTICLE pubs.aip.org/aip/jap

Multiscale computational modeling of the effects of 2'-deoxy-ATP on cardiac muscle calcium handling

Cite as: J. Appl. Phys. **134**, 074905 (2023); doi: 10.1063/5.0157935
Submitted: 12 May 2023 · Accepted: 27 July 2023 ·
Published Online: 16 August 2023

Marcus T. Hock,[1] Abigail E. Teitgen,[1] Kimberly J. McCabe,[2] Sophia P. Hirakis,[3] Gary A. Huber,[3] Michael Regnier,[4] Rommie E. Amaro,[3] J. Andrew McCammon,[3,5] and Andrew D. McCulloch[1,6,a)]

AFFILIATIONS

[1]Department of Bioengineering, University of California San Diego, La Jolla, California 92093, USA
[2]Department of Computational Physiology, Simula Resesarch Laboratory, Oslo 0164, Norway
[3]Department of Chemistry and Biochemistry, University of California San Diego, La Jolla, California 92093, USA
[4]Department of Bioengineering, University of Washington, Seattle, Washington 98109, USA
[5]Department of Pharmocology, University of California San Diego, La Jolla, California 92093, USA
[6]Department of Medicine, University of California San Diego, La Jolla, California 92093, USA

Note: This paper is part of the Special Topic on Multiscale Modeling and Analysis in Biophysics.
a)Author to whom correspondence should be addressed: amcculloch@ucsd.edu

ABSTRACT

2'-Deoxy-ATP (dATP), a naturally occurring near analog of ATP, is a well-documented myosin activator that has been shown to increase contractile force, improve pump function, and enhance lusitropy in the heart. Calcium transients in cardiomyocytes with elevated levels of dATP show faster calcium decay compared with cardiomyocytes with basal levels of dATP, but the mechanisms behind this are unknown. Here, we design and utilize a multiscale computational modeling framework to test the hypothesis that dATP acts on the sarcoendoplasmic reticulum calcium-ATPase (SERCA) pump to accelerate calcium re-uptake into the sarcoplasmic reticulum during cardiac relaxation. Gaussian accelerated molecular dynamics simulations of human cardiac SERCA2A in the E1 *apo*, ATP-bound and dATP-bound states showed that dATP forms more stable contacts in the nucleotide binding pocket of SERCA and leads to increased closure of cytosolic domains. These structural changes ultimately lead to changes in calcium binding, which we assessed using Brownian dynamics simulations. We found that dATP increases calcium association rate constants to SERCA and that dATP binds to *apo* SERCA more rapidly than ATP. Using a compartmental ordinary differential equation model of human cardiomyocyte excitation-contraction coupling, we found that these increased association rate constants contributed to the accelerated rates of calcium transient decay observed experimentally. This study provides clear mechanistic evidence of enhancements in cardiac SERCA2A pump function due to interactions with dATP.

I. INTRODUCTION

The sarcoendoplasmic reticulum calcium-ATPase (SERCA) 2A is a P-type ATPase,[1,2] which is critical for sequestration of calcium into the sarcoplasmic reticulum (SR) during cardiac relaxation and is the dominant SERCA isoform in cardiac muscle.[3] SERCA is a transmembrane protein embedded in the SR lipid membrane which consists of three cytosolic domains (nucleotide binding domain—"N," phosphorylation domain—"P," actuator domain—"A") as well as 10 transmembrane (M) helices, M1 through M10 [Fig. 1(a)].[4,5] The nucleotide binding region is located within the N domain. Calcium binding occurs in the transmembrane region between helices M4, M5, M6, and M8, at binding locations known as site I and site II [Fig. 1(c)].[5,6] Generally, SERCA transitions between two major states as it pumps calcium into the SR in an ATP-driven manner: E1 and E2. In the first state, E1, the calcium binding sites face the cytosolic side of the membrane. Binding of ATP and two calcium ions, followed by ATP dephosphorylation and hydrolysis, reconform the protein so

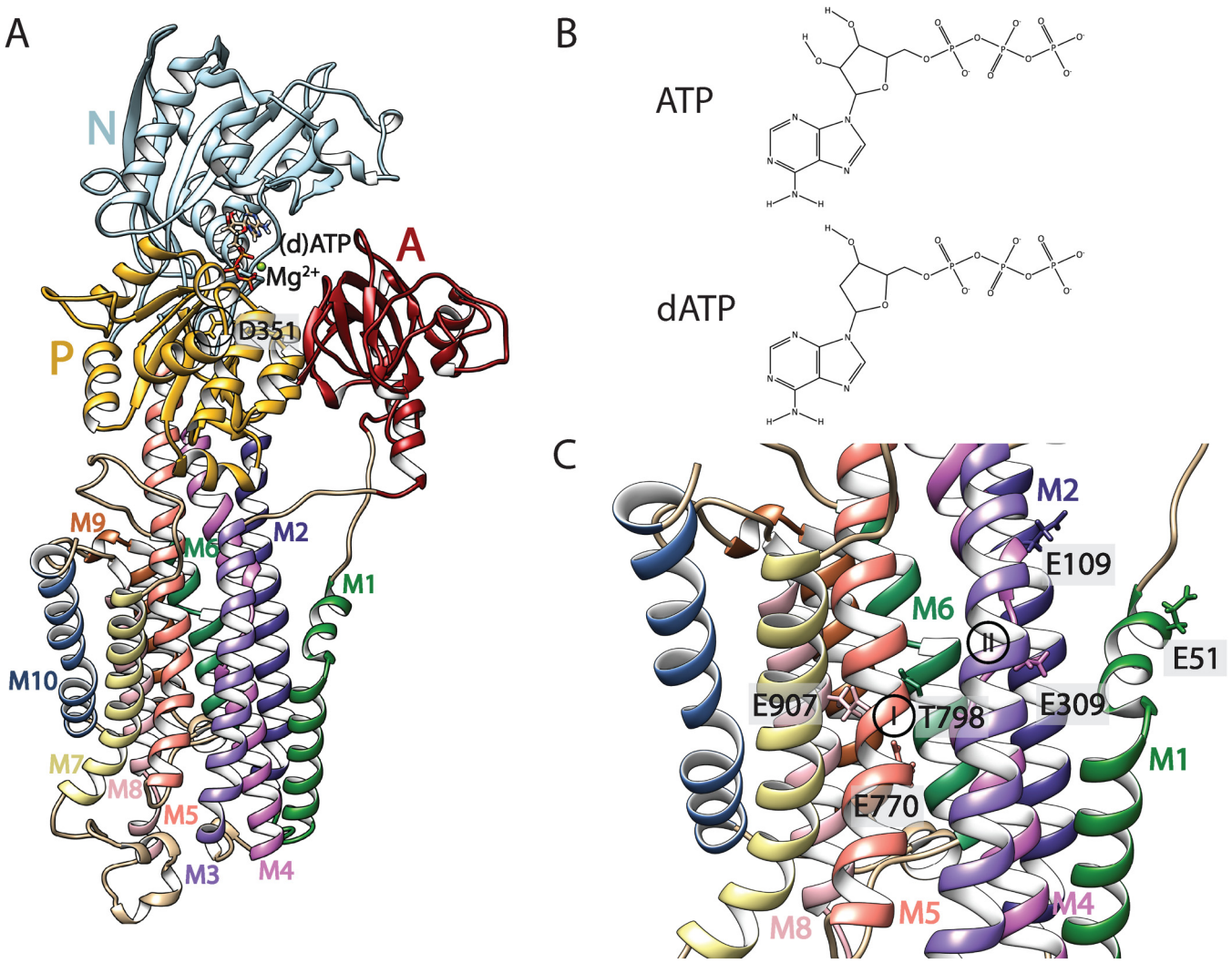

FIG. 1. (a) Overview of the SERCA structure. A, N, and P cytosolic domains, as well as M1–M10 transmembrane helices are labeled. D351, the nucleotide phosphorylation site, is also labeled. Nucleotide and Mg^{2+} are shown in the binding site on the N domain. (b) ATP and dATP chemical structures. Note missing hydroxyl group on the ribose ring for dATP. (c) Calcium binding site I and site II, and key residues used for assessing calcium binding path dynamics including E907 on M8, E770 on M5, and T798 on M6 (site I), E309 on M4 (site II), and E109 (M2) and E51 (M1) which comprise part of the calcium entry path.

that calcium can be released into the SR lumen.[5,7] The SR-facing conformation is known as E2. Release of ADP, phosphate, and calcium ions into the SR lumen allows the protein to move back into the E1 state.[5,8] A simplified ordinary differential equation model of SERCA function developed by Tran *et al.*[9] describes several rate-limiting steps within the cycle: (1) Mg^{2+}ATP binding, (2) binding of the first calcium ion to site I (site II binding is then considered to occur instantaneously), (3) ADP release, coupled with the E1–E2 transition, (4) release of calcium ions into the SR lumen, and (5) Pi release, coupled with the E2–E1 transition. Here, we focus on how the first two of these rate-limiting steps may be affected by a molecular modification to ATP.

2'-Deoxy-ATP (dATP) is a naturally occurring nucleotide that differs in structure to ATP by only a cleaved hydroxyl group on the 2' carbon of the ribose ring [Fig. 1(b)]. In spite of the similar structures of the two molecules, force production has been found to increase dramatically in cardiac cells when ATP is replaced by even a small fraction of dATP.[10,11] This finding has led to various studies exploring the potential for dATP as a therapeutic myosin activator to treat heart failure.[12–18] In one such study, upregulation of dATP to ∼1% of the overall ATP pool led to increased cell shortening, but also had a marked and beneficial effect on the calcium transient leading to improved lusitropy.[19] These results showed decreased time to 50% and 90% calcium transient decay,

suggesting that the rate of intracellular calcium reduction is enhanced during dATP treatment. This may confer additional therapeutic benefit in heart failure which is commonly characterized by decreased function and expression of SERCA2A in failing cardiac myocytes.[20–22] SERCA is also under investigation as a therapeutic target.[20,22–26] To reveal potential therapeutic mechanisms of dATP on SERCA2A, analysis at multiple scales from atomic resolution molecular dynamics to whole cell function is required.

We developed a multiscale modeling approach spanning molecular to whole cell scales. Gaussian accelerated molecular dynamics (GaMD) simulations of human cardiac E1 SERCA2A embedded in a lipid bilayer[27–30] were conducted on three separate systems: *apo*, ATP-bound, and dATP-bound. Analysis of the GaMD trajectories allowed us to locate key sites in the cytosolic and transmembrane domains of SERCA that may be modified by dATP binding. Rigid body Brownian dynamics (BD) simulations[31] were then used to measure association rate constants of ATP, dATP, and calcium ions to SERCA2A. We found that dATP bound to SERCA2A with greater affinity than ATP, and calcium bound with a higher affinity to dATP-bound than ATP-bound SERCA. Finally, in a compartmental ordinary differential equation model of whole cell calcium handling,[32] the effects of these molecular differences on the calcium transient were predicted.

II. METHODS

A. Gaussian accelerated molecular dynamics

We began with a crystal structure of human cardiac SERCA2A in the E2 state from the protein data bank (PDB) (PDB ID: 7BT2).[30,33] Since no human cardiac SERCA2A structures in the E1 state were available, we constructed a homology model using a SERCA1A crystal structure in the E1 state purified from rabbit fast-twitch skeletal muscle (PDB ID: 3W5A).[29] Homology modeling was done using SWISS-MODEL.[34] Sequence identity was 83.7%, with 93.1% similarity, determined using Clustal Omega,[35] and the GMQE score for the model was 0.77. Chain A from the 3W5A crystal structure was used for homology modeling. Ligands K^+, MPD, and PCW were removed from the 7BT2 structure, and Na^+, Mg^{2+}, M1, PTY, and sarcolipin were removed from the 3W5A structure. Nucleotide and Mg^{2+} position within the nucleotide binding pocket were taken directly from the 7BT2 structure. CHARMM-GUI was used to prepare all simulation files.[36] Protonation states were determined using the PDB2PQR PropKa tool, at a pH of 7.0.[37–40] Protonated residues were: HSE (683), and HSD (5, 32, 38, 190, 278, 284, 868, 872, 880, 882, 944). A disulfide bond was added between CYS 875 and CYS 887. The protein was embedded in a 12.5 by 12.5 nm lipid bilayer, and the position of SERCA within the bilayer was determined using the Orientations of Proteins in Membranes (OPM) database.[41] The lipid bilayer was composed of POPC (51% upper leaflet, 66% lower leaflet), POPE (43% upper leaflet, 17% lower leaflet), and POPS (6% upper leaflet, 17% lower leaflet), with 308 total lipids in the upper leaflet and 297 total lipids in the lower leaflet, based on experimentally determined membrane composition in the cardiac SR.[42] A rectangular water box of thickness 22.5 nm was added, and period boundary conditions were utilized for simulation. K^+ and Cl^- ions were added using the Monte Carlo placement method at a 150 mM concentration to neutralize the system.[43] AMBER input files were generated using CHARMM-GUI.

To construct the dATP structure, the extra hydroxyl group was removed from the ATP structure, taken directly from the 7BT2 crystal structure, using Chimera.[44] These ATP and dATP structures were then input into CHARMM-GUI, and antechamber was used to generate force field parameter files using the AMBER GAFF2 force field.[45,46] The AMBER FF19SB[47] force field was used for protein residues, and the Lipid17 and OPC[48] force fields were used for lipid and water molecules, respectively. The SHAKE algorithm was used to constrain the motion of hydrogen-containing bonds.[49]

MD and GaMD simulations were performed using Amber20,[50] and all simulations were run on the Triton Shared Computing Cluster through the San Diego Supercomputer Center.[51] A total of 150 ns of conventional MD and 200 ns of GaMD (three replicates) were performed for *apo*-SERCA, and ATP- and dATP-bound SERCA. Prior to these simulations, minimization was done over 5000 steps of steepest decent minimization with 10 kcal mol^{-1} $Å^{-2}$ positional restraints on all protein atoms and 2.5 kcal mol^{-1} $Å^{-2}$ positional restraints on all lipid atoms, with NMR restraints. Equilibration was done over six steps, for 1.875 ns total. The Langevin temperature equilibration scheme using a collision frequency of 1.0 ps^{-1} was utilized to set the system temperature to 303.15 K using the NVT ensemble over two steps (125 ps each). During these heating steps, 10 kcal mol^{-1} $Å^{-2}$ positional restraints were present on all protein atoms for the first step and 5 kcal mol^{-1} $Å^{-2}$ positional restraints were present on all protein atoms for the second step, and 2.5 kcal mol^{-1} $Å^{-2}$ positional restraints with NMR restraints were present on all lipid atoms for both steps. The system was then equilibrated over four stages using the semi-isotropic (with constant surface tension) NPT ensemble (constant number of particles, pressure, and temperature), for 125, 500, 500, and 500 ps, respectively, with the system set to 1.0 bar. Positional restraints on all protein atoms were 2.5, 1.0, 0.5, and 0.1 kcal mol^{-1} $Å^{-2}$ for each step, respectively. Positional and restraints on all lipid atoms were 1.0, 0.5, 0.1, and 0 kcal mol^{-1} $Å^{-2}$ for each step, respectively, with NMR restraints.

MD and GaMD simulations were run at 303.15 K using the PMEMD (particle mesh Ewald molecular dynamics) method with a 9 Å nonbonded cutoff, and 2 fs time step. Coordinates were saved every 100 ps for MD and 20 ps for GaMD simulations. In GaMD, a Gaussian distribution is used to provide a boost potential for the system in order to enhance conformational sampling at shorter simulation time scales.[27] A single boost potential was applied to the total potential energy only. The final frame from the 150 ns MD simulations was used as the starting point for the GaMD simulations, and 0.4 ns of conventional MD prep, 2.4 ns of conventional MD (to calculate potential statistics), 0.4 ns of GaMD pre-equilibration (with boost potential applied), and 10.4 ns of GaMD equilibration (with boost potential applied and boost parameters updated) were run before all GaMD production simulations. The three GaMD replicates were averaged for analysis. Chimera, VMD, and PyMol were used for trajectory analysis and visualization.[44,52,53] Analysis was performed using the AMBER cpptraj[54] and the MDTraj python libraries.[55] Hydrogen bonding analysis used a 3 Å and 135° cutoff. Energetic reweighting of trajectory data was performed after all simulations using a Gaussian

approximation of cumulant expansion to the second order. This step is necessary because a boost potential was applied at each time step in order to flatten the energy landscape during the simulation and increase conformational sampling.[27] Briefly, the potential for mean force (PMF) as a function of reaction coordinate A_j is calculated as:

$$PMF(A_j) = -\frac{1}{\beta}\ln p(A_j), \tag{1}$$

where $\beta = k_B T$ and $p(A_j)$ is the canonical ensemble distribution. Because boost potentials followed a Gaussian distribution, $p(A_j)$ must be calculated from the ensemble distribution of the boosted data set as

$$p(A_j) = p^*(A_j)\frac{\langle e^{\beta\Delta V(r)}\rangle_j}{\sum_{j=1}^{M}\langle e^{\beta\Delta V(r)}\rangle_j}\ln p(A_j), \quad J = 1, \ldots, M, \tag{2}$$

where $\Delta V(r)$ is the boost potential for each frame, M is the number of bins, and $\langle e^{\beta\Delta V(r)}\rangle_j$ is the ensemble averaged Boltzmann factor for frames in bin j. $\langle e^{\beta\Delta V(r)}\rangle$ is approximated using second order cumulant expansion and is calculated as

$$\langle e^{\beta\Delta V(r)}\rangle = \exp\left\{\sum_{k=1}^{\infty}\frac{\beta^k}{k!}\sigma_{\Delta V}^2\right\}. \tag{3}$$

Re-weighting of the GaMD simulations was done using scripts and protocols developed by Miao *et al.*[56]

B. Brownian dynamics

BD simulations with Browndye 2[31] were used to probe SERCA binding kinetics. Browndye treats molecules as rigid cores and uses an adaptive time step to efficiently simulate binding kinetics. We first carried out BD simulations of ATP and dATP binding to the *apo* SERCA structures derived from our GaMD simulations and compared their respective association rate constants. In order to better capture the conformational dynamics and variability of SERCA, 30 SERCA structures were used independently in 30 separate simulations for ATP and dATP. The 30 conformations were obtained through hierarchical clustering of the *apo* GaMD SERCA simulations, using C_α RMS as the cutoff metric. The lipid bilayer was removed for nucleotide binding simulations to reduce simulation compute cost, given that the bilayer should not substantially affect the relative rates of binding of ATP and dATP. Browndye uses "reaction pairs" as a reaction coordinate to measure progress of binding events. These pairs were defined based on the starting homology model with ATP or dATP present. Pairs were defined by contacts between (d)ATP and residues PHE 487 and ARG 559 with a distance less than 3.5 Å. The full list of binding pairs can be found in Table S1 and is further illustrated in Fig. S1 in the supplementary material. The encounter complex description in Browndye, which specifies the distance between pairs necessary for a reaction to be considered complete, was left unspecified, allowing for a range of binding probabilities to be observed as a function of reaction distance. For each of the 30 representative structures, BD simulations were carried out to measure the association of ATP, and separately with dATP, with 50 000 individual trajectories simulated per conformation. Overall, 1.5 million total ATP trajectories were simulated as well as 1.5 million dATP trajectories. The same AMBER force field used for the GaMD simulations was used to parameterize the protein and nucleotide charges and radii for BD simulations. Binding rate constant curves of the resulting simulations were then averaged based on the cluster weight of each observed representative structure.

We again employed BD simulations to investigate changes in calcium binding to site I and II in SERCA when ATP or dATP is bound. The starting SERCA structures were clustered from the GaMD ATP and dATP simulations. Thirty representative structures were extracted from each nucleotide condition, with the membrane intact. The same hierarchical clustering approach based on the C_α RMS was again applied to generate representative structures. The membrane was included to ensure that calcium enters the SERCA protein through a realistic entry point, likely via the M1/M2/M4 path, and not through the transmembrane region buried in the lipid bilayer.[5] Reaction pairs for calcium to site I were defined based on atoms forming hydrogen bonds in a previously solved crystal structure.[57] A second set of reaction pairs was also established from the same crystal structure for site II (full list for site I and II can be found in Table S2 in the supplementary material). For site I, the 30 structures from the ATP conditions were used to run 50 000 BD trajectories, leading to 1.5 million trajectories. Similarly, the 30 structures from the dATP GaMD simulations were used to run an additional 50 000 BD trajectories per conformation, again leading to 1.5 million trajectories simulated. The binding rate constant curves were averaged based on the frequency of the cluster throughout the GaMD simulations. The same procedure was repeated using the same structures to investigate binding to site II, with the reaction pairs adjusted accordingly for an additional 1.5 million trajectories per nucleotide condition. In total, between the two calcium sites and two nucleotides bound, 6 million calcium binding BD trajectories were simulated.

All BD simulations for both the nucleotide and calcium association simulations used 150 mM ionic strength, and a desolvation parameter of 0.025 based on sensitivity analysis to allow for realistic binding distance criteria. Each BD trajectory had a maximum of 1 000 000 steps. The dielectric coefficient of the solvent was set to 78, while the solute dielectric coefficient was set to 4.

C. Calcium transient modeling

To assess how changes in nucleotide and calcium association rate constants to SERCA impact the myocyte calcium transient as a whole, we utilized a whole cell excitation-contraction coupling (ECC) model developed by Himeno *et al.*[32] This model was chosen because it explicitly includes a three-state model of SERCA[9] which has parameters for ATP binding, calcium binding, and E1–E2 transition. In this model, state P_1 is E1 SERCA, which undergoes a reversible reaction dictated by rates K_1^+ and K_1^- to state P_{2-5} (E1 with ATP and 2 calcium ions bound). Calcium binding is considered to be fully cooperative, i.e., binding of the second calcium ion is instantaneous after the first calcium binding event. Reaction rates K_2^+ and K_2^- encompass MgADP dissociation as well as the E1–E2

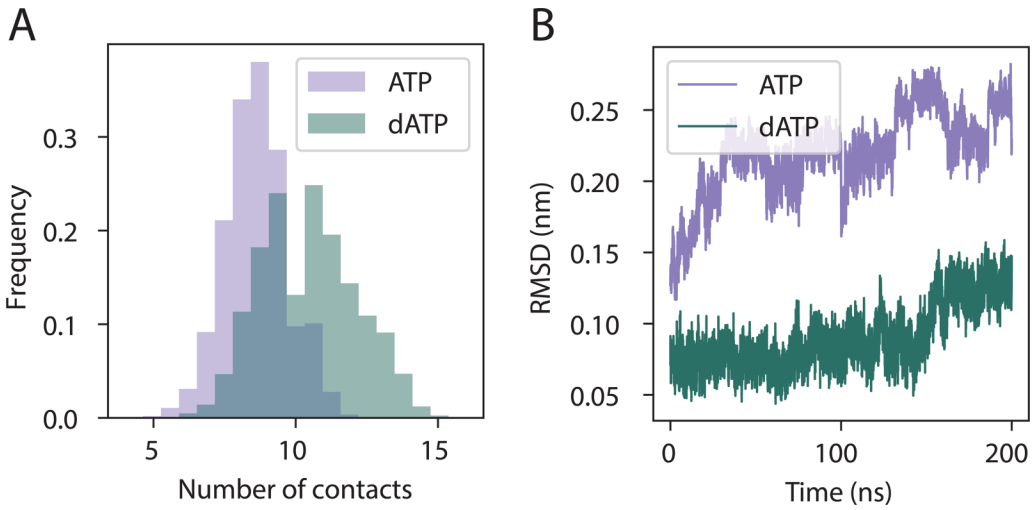

FIG. 2. dATP is more stable in the nucleotide binding pocket. (a) The overall number of contacts in the binding pocket (averaged across three replicates) was greater for dATP than for ATP. Only residues identified to come within 3 Å for at least one frame of the simulation were included. Data are displayed as histograms showing the frequency distribution across the GaMD simulations. (b) The RMSD for dATP (averaged across 3 replicates) was lower than for ATP.

transition, leading the model to state P_{6-10}. Finally, reversible reaction rates K_3^+ and K_3^- return the pump to state P_1.[9] dATP experimental data were digitized from Korte *et al.* Fig. 1(b) (GFP and R1R2, respectively).[19] Fura ratio units were converted to calcium concentration by setting the maximum fluorescence value to 0.45 μM, and the minimum value to 0.05 μM, since these are approximately the maximum and minimum calcium values typically seen in the ECC model.[32] The ECC model was optimized to match the ATP experimental calcium transient by varying Amp_{SERCA}, Amp_{NCX}, Amp_{NaK}, and f_n, the same parameters which were tuned by Himeno *et al.* in parameterizing their original model.[32] Optimization was conducted using Particle Swarm Optimization in MATLAB.[58] The timescale of the applied current in the ECC model was adjusted to reflect differences between human and rat and to more closely fit control (ATP) calcium transients.

III. RESULTS

A. dATP is more stable in the nucleotide binding pocket, facilitating E1-ATP to E1-ADP transition via enhanced phosphorylation and movement of cytosolic domains

We first assessed differential interactions of ATP and dATP in the nucleotide binding pocket in the N domain. Computing the overall number of contacts between the nucleotide and residues identified to come within 3 Å for at least one frame of any of the simulations, we found that dATP had a greater number of contacts overall [Fig. 2(a)]. The average number of contacts was 8.7 for ATP and 10.5 for dATP. Further, we found that dATP had a lower RMSD overall (averaged across all three GaMD simulations) than ATP [Fig. 2(b)]. This suggests that dATP is interacting more closely with a greater number of residues in the N domain binding pocket, and that it binds more stably, leading to less movement within the binding pocket.

We next assessed specific residue interactions with ATP and dATP in the nucleotide binding pocket. The distances across three GaMD replicates between the nucleotide and several residues of interest are shown in Fig. 3(a). Distances to known nucleotide interaction residues PHE 487, ARG 559, and LYS 514[5,59–61] were unchanged (the average distances were 0.39 nm, 0.30 nm, and 0.47 nm for ATP and 0.39 nm, 0.26 nm, and 0.45 nm for dATP, respectively). This suggests that interactions with these residues do not explain differences in nucleotide association. However, we found that ATP came in closer contact with several residues toward the top of the nucleotide binding pocket than dATP, including THR 441, LYS 492, ARG 677, and ARG 489 (average distances were 0.50 nm, 0.33 nm, 0.36 nm, and 0.43 nm for ATP and 0.56 nm, 0.39 nm, 0.53 nm, and 0.49 nm for dATP, respectively) [Fig. 3(b)]. The phosphate tail of dATP was shown to come in closer contact with several residues toward the bottom of the nucleotide binding pocket than ATP, including LYS 352, THR 353, THR 624, and ASP 626 (average distances were 0.83 nm, 0.95 nm, 0.91 nm, and 0.56 nm for ATP and 0.45 nm, 0.47 nm, 0.41 nm, and 0.42 nm for dATP, respectively) [Fig. 3(c)]. We hypothesize that this is due to the additional hydroxyl group on ATP [Fig. 1(b)], allowing it to form additional hydrogen bonding interactions with residues at the top of the binding pocket, while dATP does not, causing the phosphate tail to be pulled downwards. The hydrogen bond occupancy of the 2' hydroxyl group on ATP was measured to be 8.21% as a hydrogen bond acceptor, 4.80% as a donor, and overall acting as either a donor or acceptor in 12.4% of the simulation. While this is a minority of the simulation time, the consistent interaction significantly alters its orientation and behavior in the

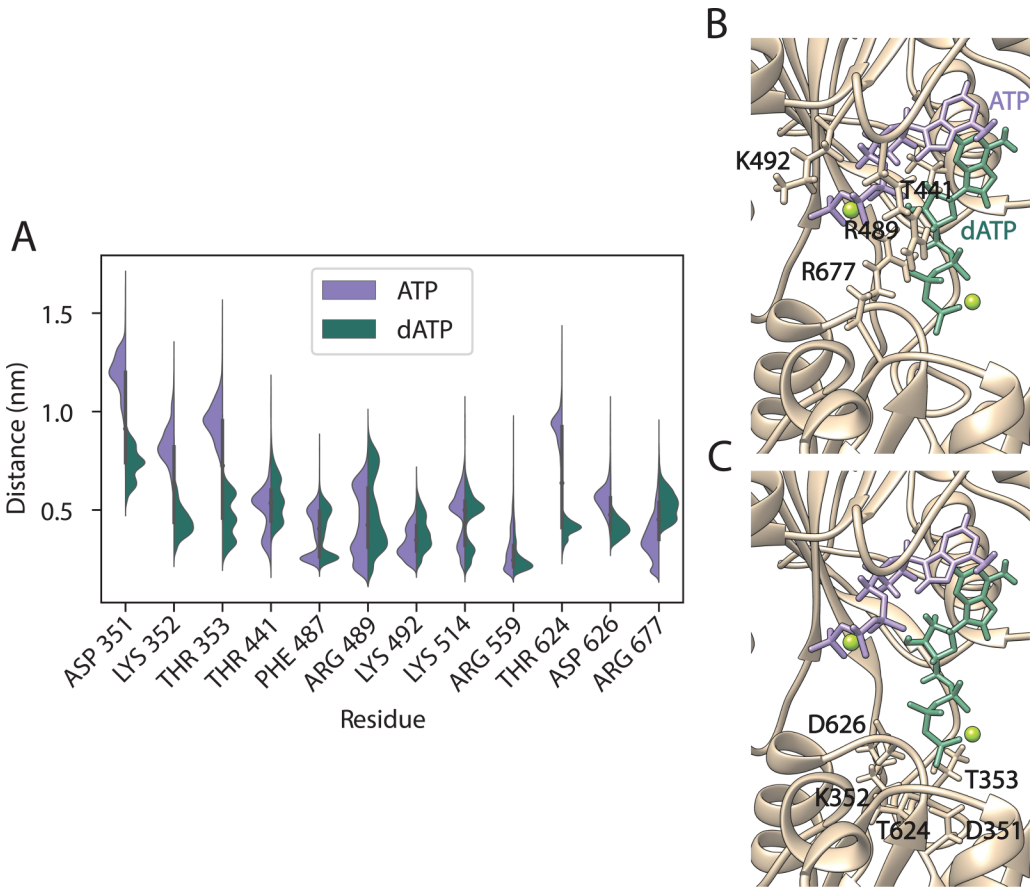

FIG. 3. dATP occupies a more vertically aligned conformation in the binding pocket than ATP. (a) Distance between nucleotide and residues of interest for ATP and dATP (averaged across three replicates). For each residue of interest, distance distributions (between the residue and nucleotide) are shown as violin plots, where the white dot in the center represents the median, and the thick gray bar represents the interquartile range. Density curves are shown for ATP on the left side of the plot and dATP on the right side of the plot, where the width of the curve represents the frequency of the data (nucleotide-residue distance) at that point. ATP came in closer contact with residues toward the top of the binding pocket, including THR 441, LYS 492, ARG 677, and ARG 489 [shown in (b)]. dATP was shown to come in closer contact with residues toward the bottom of the binding pocket including LYS 352, THR 353, THR 624, ASP 626, and phosphorylation residue ASP 351 [shown in (c)]. This may be explained by the missing hydroxyl group on dATP leading to weaker interactions with residues at the top of the binding pocket. Distances to nucleotide association residues PHE 487 and ARG 559, as well as LYS 514, were unchanged.

pocket. The preserved 3' hydroxyl shows similar levels of hydrogen bonding occupancy between ATP and dATP, at 30.4% and 34.8% occupancy, respectively, as either a donor or acceptor. Interestingly, in dATP, the 3' hydroxyl almost never bonds as a donor, at only 0.0312% of frames compared to 4.92% in ATP. These results are further supported by clustering analysis, which confirmed that ATP is most commonly located more horizontally across the top portion of the binding pocket across all 3 replicates, while dATP shows a more vertically aligned conformation in which the phosphate tail is drawn downwards toward the P domain (Fig. S2 in the supplementary material). This serves to position dATP such that the gamma phosphate is located substantially closer to the phosphorylation residue ASP 351 (average distance was 1.2 nm for ATP and 0.74 nm for dATP) [Figs. 3(a) and 3(c)].[5] This may allow for faster phosphorylation by dATP compared with ATP.

Finally, we assessed the differential effects of ATP and dATP on the movement of cytosolic domains of SERCA2A. Closure of the A and N domains [Fig. 1(a)], in particular, is important for the E1-ATP to E1-ADP transition.[2,5,62] We found that the average difference between the center of mass of the A and N domains was smaller for dATP than for ATP (average distance was 3.8 nm for ATP and 3.5 nm for dATP), suggesting that dATP enhances closure of these domains [Fig. 4(a)]. Further, the standard deviation in A-N domain distances was smaller for dATP than ATP (0.09 nm for ATP vs 0.08 nm for dATP), suggesting that dATP may also stabilize these domains in a more closed conformation. This was also shown to correspond to the first principal component from a PCA analysis conduced on SERCA structures from the GaMD simulations [Fig. 4(b)], suggesting that this is the major motion captured by our simulations. Further, reweighting analysis confirmed that

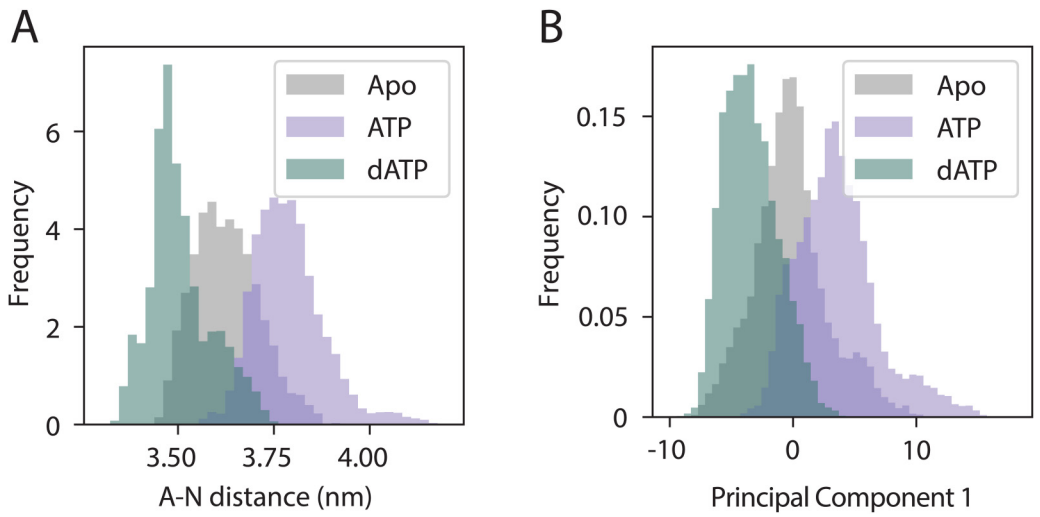

FIG. 4. dATP enhances transition from E1-ATP to E1-ADP via A-N domain closure. Data are displayed as histograms showing the frequency distribution across the GaMD simulations. (a) A-N domain distance (averaged across three replicates), measured from the center of mass for each domain, was lower for dATP than ATP. (b) First principal component from PCA analysis of C_α movement performed on GaMD trajectories, which corresponds to A-N domain movement.

these effects were not due to bias in the GaMD simulations since the decrease in A-N distance with dATP, represented by a minimum in the Potential of Mean Force (PMF), was still present even after recovering the original energy landscape (without the GaMD boost potential) via reweighting (Fig. S3 in the supplementary material). Interestingly, ATP increased A-N domain distances with respect to the *apo* structure, while dATP decreased A-N domain distances with respect to the *apo* structure. This may be due to the fact that our GaMD simulations do not have calcium present; in the absence of calcium, the nucleotide can bind to the N domain and can lead to opening of the cytosolic domains, but cannot lead to subsequent complete closure of these domains or phosphorylation.[5,30] The effects of dATP on SERCA appear to be pronounced enough to lead to greater closure of the A and N domains. We expect that if calcium was present in the GaMD simulations, ATP A-N distances would be smaller than the *apo* case, and dATP A-N distances would be decreased even further.

B. dATP binding to SERCA leads to opening of calcium binding path

Next, we assessed whether dATP binding affects calcium association in the transmembrane region. The calcium binding sites have been shown to be allosterically linked to the nucleotide binding site via transmembrane helix M5.[5] Calcium binds first to site I (passing through site II, which is gated by GLU 309).[2,5,63,64] This is believed to occur through a cooperative mechanism, where binding of calcium to site I increases calcium binding affinity for site II.[63,65,66] We computed distances between THR 798 (M6), GLU 770 (M5), and GLU 907 (M8), since these residues make up calcium binding site I[5] [Fig. 1(c)]. We found that the average distances between M5 and M6 were increased (average distances were 0.55 nm for ATP and 0.66 for dATP) [Fig. 5(a)]. Average distances between M5 and M8 were also increased (average distances were 0.45 nm for ATP and 0.52 nm for dATP) [Fig. 5(b)]. Average distances between M6 and M8, on the other hand, were decreased (average distances were 0.26 nm for ATP and 0.25 nm for dATP) [Fig. 5(c)]. This suggests that the net effect of dATP is to cause opening of calcium binding site I, since M5-M6 and M5-M8 distances were increased by a greater magnitude than M6-M8 distances were decreased with dATP. Similar to the effects of dATP on A-N domain distances, here we observed again that ATP and dATP had opposing effects on transmembrane helix distances with respect to the *apo* structure. This may again be due to the fact that our GaMD simulations were carried out in the absence of calcium.

Further, we assessed the effects of dATP on calcium entry. Calcium is proposed to enter SERCA through two different paths.[63,67] The first is composed of M6, M7, M8, and M9, while the second is composed of M1, M2, and M4. We chose to focus on the second, since there is greater evidence supporting this path.[67–70] We assessed distances between GLU 51 (M1) and GLU 109 (M2), residues which have been implicated in calcium sensing and compose part of the binding path[67] [Fig. 1(c)], and found that dATP also led to an increase in this distance (average distance was 0.88 nm for ATP and 0.94 nm for dATP) [Fig. 5(d)]. We again verified that these results were not due to bias in the GaMD simulations by conducting a reweighting analysis since the changes in residue distances with dATP, represented by a minimum in the Potential of Mean Force (PMF), were still present even after recovering the original energy landscape (without the GaMD boost potential) via reweighting (Fig. S4 in the supplementary material). Further, the standard deviation of the distance distribution was smaller for dATP than ATP (0.11 nm for ATP and 0.06 nm for dATP), suggesting that dATP also acts to stabilize these residues in

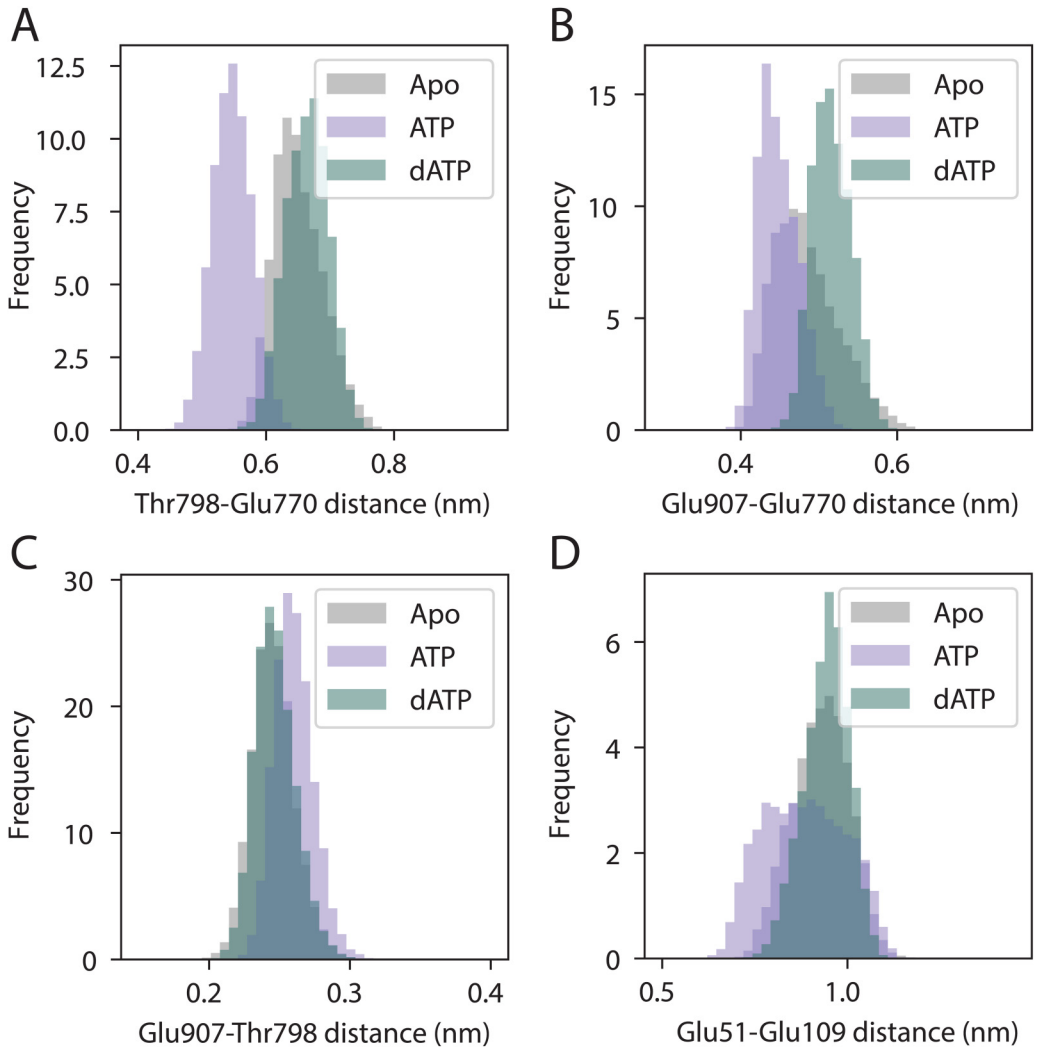

FIG. 5. dATP binding leads to rearrangement of calcium binding path. Distances for key residues on M5 (GLU 770), M6 (THR 798), and M8 (GLU 907) that make up calcium binding site I, as well as calcium sensing residues on M1 (GLU 51) and M2 (GLU 109) that make up the calcium entry path are shown. Distances were averaged across 3 replicates. Data are displayed as histograms showing the frequency distribution across the GaMD simulations. Distances between M5 and M6 (A) and M5 and M8 (B) were increased, while distances between M6 and M8 (C) were decreased with dATP. Distances between M1 and M2 were increased with dATP (D). This suggests that dATP may facilitate calcium binding by opening the calcium entry path to site I.

a more open position. Thus, dATP may lead to opening of both the calcium binding path and calcium binding site I, which could facilitate enhanced calcium association.

C. dATP increases rates of nucleotide and calcium association to SERCA compared with ATP

BD simulations revealed that dATP bound more rapidly to the *apo* structure of SERCA compared with ATP. The weighted average binding curve shows that across a wide range of reaction distances greater than 7 Å, dATP binds more rapidly to the *apo* structure than ATP [Figs. 6(a) and 6(b)]. Selecting a reaction distance of 8.11 Å corresponding to the ATP binding rate constant of $2.59 \times 10^7\ (\mathrm{M\,s})^{-1}$ used by Tran *et al.*,[9] the corresponding dATP association rate constant was 36% higher [$3.52 \times 10^7\ (\mathrm{M\,s})^{-1}$]. We attribute the lower dATP binding rate constants at low reaction distances to noise, since very few BD simulations reached these small distances. Less than 0.05% of simulations reached a distance of less than 8 Å and less than 0.03% of reactions reached a distance of less than 5 Å. Although ATP does have an additional polar hydroxyl group that may promote additional electrostatic attraction to the nucleotide binding pocket, we anticipate that removal of this

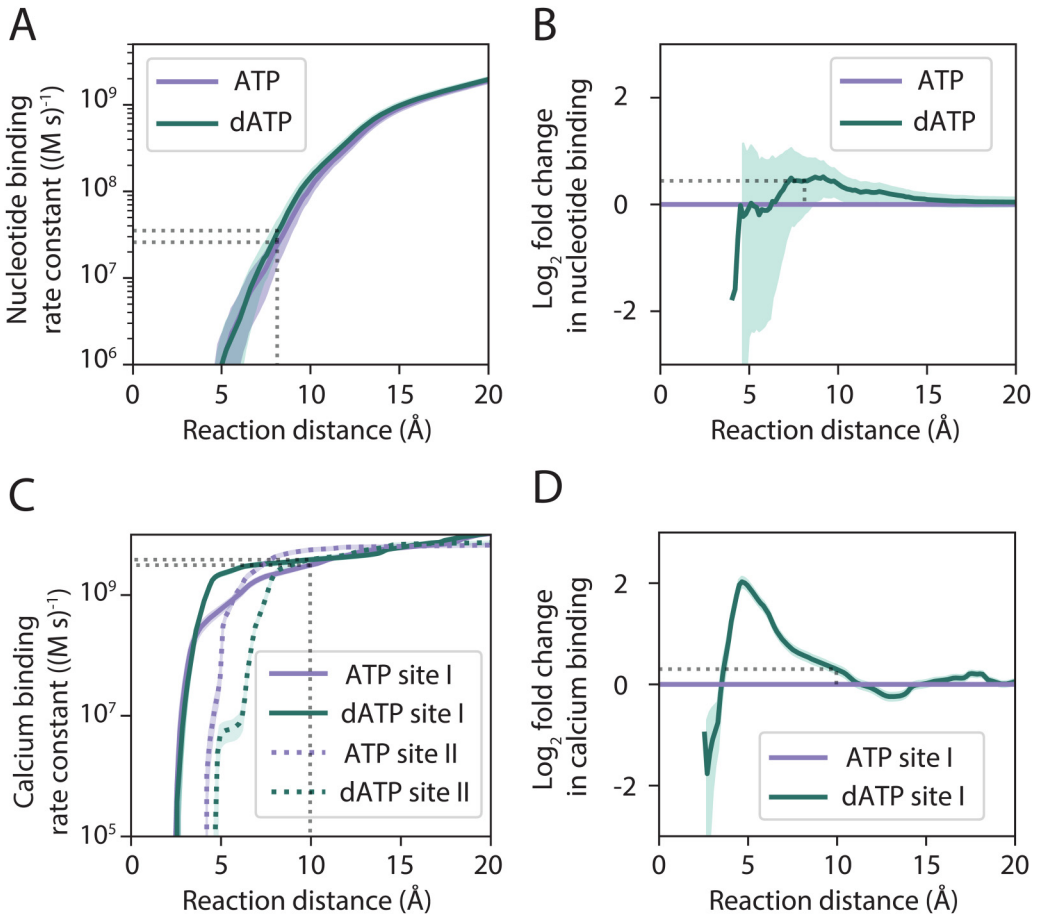

FIG. 6. (a) BD-predicted binding rate constants as a function of reaction distance. Dotted lines represent reaction distance for association rate constant of ATP to SERCA used in the Tran *et al.* model.[9] (b) Log_2 fold change in nucleotide binding rate constant as a function of reaction distance. Log_2 fold change is used to more easily visualize changes in binding rate constant e.g., a doubling of the binding rate constant is equivalent to a $\log_2$ fold change of 1, quadrupling is equivalent to a $\log_2$ fold change of 2, etc. Log fold changes of less than 1 are negative while fold changes greater than 1 are positive (e.g., a halving of the binding rate constant is equivalent to a $\log_2$ fold change of -1). dATP binds more rapidly to the nucleotide site for reaction distances greater than 7 Å below which sampling errors increase owing to the low number of simulations reaching lower reaction distances. (c) BD-predicted association rate constant of calcium to sites I and II. dATP increases calcium binding to site I compared with ATP. Calcium binds site II more rapidly when ATP is bound to SERCA than dATP. Dotted lines represent reaction distance that corresponds to the calcium association rate constant determined from a previous BD study.[67] (d) Log_2 fold change in the association rate constant of calcium to site I when dATP is bound compared with ATP.

functional group reduces steric hindrance, therefore allowing dATP easier access to the binding site, and that this effect dominates the BD simulations. Furthermore, analysis of a structure by structure comparison of the 30 SERCA conformations used in our simulations revealed that although the nucleotide binding rate constant varied considerably from conformation to conformation, dATP consistently associated more rapidly to SERCA compared with ATP.

Further, BD simulations of dATP-bound SERCA showed differences in calcium binding compared to ATP-bound SERCA [Figs. 6(c) and 6(d)]. For reaction distances between 4 and 12 Å, calcium bound more rapidly to site I when dATP was bound than ATP. Experimental estimates of calcium association rate constants to SERCA vary by up to three orders of magnitude, making determining an absolute binding distance and rate constant difficult, however a previous BD study estimated a calcium association rate constant of $3.13 \times 10^9\,(\text{M s})^{-1}$ to ATP-bound SERCA.[67] In our simulations, this value corresponded to a reaction distance of 10 Å at which calcium binding to site I of dATP-bound SERCA was 23% greater [$3.85 \times 10^9\,(\text{M s})^{-1}$]. Interestingly, dATP reduced the association rate constant of calcium to site II. It is believed that calcium binds to site I first and initiates a conformational change before a second calcium ion can bind to site II. Therefore, the structures extracted from our GaMD simulations may not be an accurate representation of SERCA when the first calcium ion is bound. This process is also cooperative, so we anticipate that this sequential step

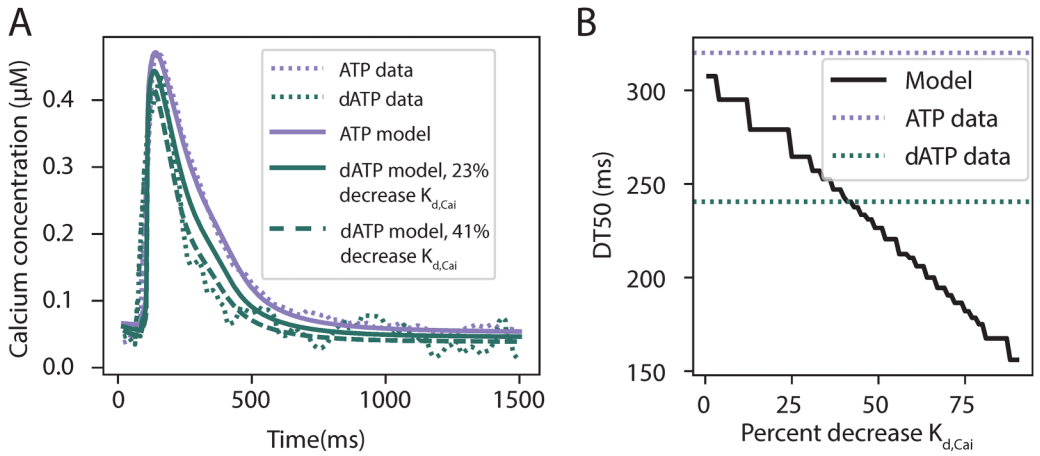

FIG. 7. dATP accelerates the rate of myocyte calcium transient decay via enhanced calcium association. (a) Effects of changing model parameters K_1^+ and $K_{d,Cai}$ (nucleotide and calcium association rate constants, respectively) in the Tran model.[9] ATP and dATP experimental data digitized from Korte *et al.*[19] are shown as dotted lines. ATP model calcium transient (optimized to match ATP experimental data), and dATP predicted model calcium transients for 36% increase in K_1^+ combined with 23% and 41% decreases in $K_{d,Cai}$ are also shown. (b) Percent decrease in $K_{d,Cai}$ vs DT50. With a 23% decrease in $K_{d,Cai}$ (based on BD results), we are not able to fully match experimental measurements. However, with a 41% decrease in $K_{d,Cai}$, we are able to match experimental measurements of DT50 with dATP. These simulations also include a 36% increase in K_1^+ based on BD results, but changes in K_1^+ were not shown to substantially affect DT50 (Fig. S5 in the supplementary material).

significantly alters the binding kinetics of the second calcium ion. As such, we focus our subsequent multiscale analysis on the effects of dATP on calcium binding to SERCA at site I.

D. Enhanced calcium binding to dATP-bound SERCA accelerates myocyte calcium transient decay

We optimized parameters of the Himeno ECC model to match measured calcium transients in the presence of ATP, as described in the methods.[19,32,58] In the Tran model of SERCA kinetics[9] (incorporated within the Himeno model), K_1^+ (rate of ATP binding to SERCA) and $K_{d,Cai}$ (dissociation constant for calcium binding to SERCA) were then adjusted based on the results of the BD simulations. Thus, K_1^+ was increased from $2.59 \times 10^7\,(\mathrm{M\,s})^{-1}$ to $3.52 \times 10^7\,(\mathrm{M\,s})^{-1}$ based on the BD-predicted change in nucleotide association to SERCA, and $K_{d,Cai}$ was was decreased by 23% from 0.0027 to 0.0021 mM based on the BD-predicted change in calcium binding to site I. These changes decreased time to 50% decay (DT50) of the calcium transient, but only modestly from 308 to 279 ms [Fig. 7(a)]. However, decreasing $K_{d,Cai}$ by 41%, which is still within the range of the BD simulation results, shortened DT50 by an amount similar to experimental observations in the presence of dATP [Fig. 7(b)]. In contrast, changes in the nucleotide association rate constant had little effect, suggesting that increasing calcium binding to site I may be the primary mechanism by which dATP increases SR calcium reuptake (Fig. S5 in the supplementary material).

IV. DISCUSSION

The results of this study provide new evidence for mechanisms by which dATP treatment may contribute to improved SERCA pump function in cardiac myocytes. First, dATP was shown to be more stable in the binding pocket of SERCA and was positioned to facilitate faster phosphorylation. Increased separation of the A-N cytosolic domains indicates faster pump function with dATP treatment. Further, we observed separation of transmembrane helices M5 and M6 and M5 and M8, as well as M1 and M2, which may facilitate faster calcium association. dATP demonstrates a 36% higher association rate constant than ATP to the N domain of SERCA. However, inputting the nucleotide and calcium association rate constants determined from BD analysis (K_1^+ and $K_{d,Cai}$) into an ECC model did not fully explain experimentally observed differences in the calcium transient due to dATP, but further decreasing the calcium dissociation constant could.

While this study provides valuable insight into the molecular mechanisms by which dATP affects SERCA function, our GaMD simulations did not capture the phosphorylation event or downstream protein conformational changes after calcium binding. Future molecular dynamics or quantum mechanics simulation studies would aid in better elucidating these effects. Our BD simulations also allowed for the entry of the nucleotides and calcium from any orientation from the SERCA pump, not only the cytosolic side, which is a limit of our approach. Moreover, there are also other ATPases that contribute to intracellular calcium dynamics such as the Plasma Membrane Calcium-ATPase (PMCA) and the Sodium-Potassium ATPase exchanger (NaK) which may also be affected by dATP to enhance calcium efflux from the cell. SERCA is regulated by phospholamban and several post-translational modifications that could also affect its pump function.[22] It is likely that both SERCA upregulation and these other pumps together could explain the improved relaxation observed experimentally due to dATP treatment. This could be further explored with computational and experimental studies that specifically focus on the effects of the cooperative binding of Ca^{2+} with relation to dATP and ATP.

For instance, additional MD simulations of SERCA with one or both Ca^{2+} binding sites occupied will certainly change the free-energy landscape and thus, yield additional structures and insights. Additionally, since dATP is a candidate therapeutic approach for heart failure with reduced ejection fraction, which is characterized by prolonged twitch relaxation and calcium transient decay associated with downregulated SERCA function, it would be useful to apply this analysis to a model of ECC in the failing cardiac myocyte.

In this study, we analyzed the effects of nucleotide binding on SERCA pump kinetics and the differential effects of ATP and dATP on calcium affinity via changes to the transmembrane domain. This study has demonstrated the power of multiscale modeling for investigating the effects of ATP analogs on cardiac cells, as we integrated knowledge from the atomic to the cellular level to uncover potential mechanisms of dATP which scale up to a significantly altered calcium transient and cardiac function as a whole.

SUPPLEMENTARY MATERIAL

See the supplementary material for the nucleotide atom labeling and atom pairs used for the Brownian dynamics simulations. Additional figures show nucleotide clustering from the GaMD simulations and reweighted PMF measurements of conformational changes based on the applied boost potential. The supplementary material also includes a sensitivity analysis of parameters altered in the ECC model.

ACKNOWLEDGMENTS

This work is supported by the American Heart Association under Grant No. 906494 to M.T.H., National Science Foundation Graduate Research Fellowship Program under Grant No. DGE-2038238 to A.E.T., NIH grant GM31749 to G.H., and also supported by a gift from the Wu Tsai Foundation to the Human Performance Alliance. S.P.H. was funded through a fellowship from the Interfaces Graduate Training Program (No. NBIB T32 EB009380). The research was funded in part by the National Institutes of Health (NIH) through the NIH Director's New Innovator Award Program (DP2-OD007237 to R.E.A.) and an NSF XSEDE/ACCESS supercomputer resources grant (CHE060073N to R.E.A) from the National Biomedical Computation Resource (NBCR) and NIH P41 GM103426. We would also like to thank the San Diego Supercomputer Center for a computing time allocation on the Triton Shared Computing Cluster.

AUTHOR DECLARATIONS

Conflict of Interest

A. D. McCulloch is a co-founder of Vektor Medical Inc. and Insilcomed Inc., neither of which were involved either directly or indirectly in any way with this research.

Author Contributions

Marcus T. Hock, Abigail E. Teitgen, and Kimberly J. McCabe contributed equally to this paper.

Marcus T. Hock: Conceptualization (equal); Formal analysis (equal); Writing – original draft (equal); Writing – review & editing (equal). **Abigail E. Teitgen:** Conceptualization (equal); Formal analysis (equal); Writing – original draft (equal); Writing – review & editing (equal). **Kimberly J. McCabe:** Conceptualization (equal); Formal analysis (equal); Writing – original draft (equal); Writing – review & editing (equal). **Sophia P. Hirakis:** Conceptualization (equal); Writing – review & editing (equal). **Gary A. Huber:** Software (lead); Writing – review & editing (equal). **Michael Regnier:** Conceptualization (equal); Writing – review & editing (equal). **Rommie E. Amaro:** Conceptualization (equal); Writing – review & editing (equal). **J. Andrew McCammon:** Conceptualization (equal); Resources (supporting); Writing – review & editing (equal). **Andrew D. McCulloch:** Conceptualization (equal); Resources (equal); Writing – review & editing (equal).

DATA AVAILABILITY

The data that support the findings of this study are openly available at http://gpcrmd.org. Analysis scripts can be found at https://github.com/marcushock/serca-atp-datp.

REFERENCES

[1]M. G. Palmgren and P. Nissen, Annu. Rev. Biophys. **40**, 243 (2011).
[2]M. Brini and E. Carafoli, Physiol. Rev. **89**, 1341 (2009).
[3]G. Inesi, A. M. Prasad, and R. Pilakatta, Biochem. Biophys. Res. Commun. **369**, 182 (2008).
[4]T. L.-M. Sørensen, J. V. Møller, and P. Nissen, Science **304**, 1672 (2004).
[5]C. Toyoshima, Arch. Biochem. Biophys. **476**, 3 (2008).
[6]D. M. Clarke, T. W. Loo, G. Inesi, and D. H. MacLennan, Nature **339**, 476 (1989).
[7]C. Olesen, T. L.-M. Sørensen, R. C. Nielsen, J. V. Møller, and P. Nissen, Science **306**, 2251 (2004).
[8]M. Bublitz, M. Musgaard, H. Poulsen, L. Thøgersen, C. Olesen, B. Schiøtt, J. P. Morth, J. V. Møller, and P. Nissen, J. Biol. Chem. **288**, 10759 (2013).
[9]K. Tran, N. P. Smith, D. S. Loiselle, and E. J. Crampin, Biophys. J. **96**, 2029 (2009).
[10]M. Regnier, A. J. Rivera, Y. Chen, and P. B. Chase, Circ. Res. **86**, 1211 (2000).
[11]M. Regnier, H. Martin, R. J. Barsotti, A. J. Rivera, D. A. Martyn, and E. Clemmens, Biophys. J. **87**, 1815 (2004).
[12]B. Schoffstall, A. Clark, and P. B. Chase, Biophys. J. **91**, 2216 (2006).
[13]S. G. Nowakowski, S. C. Kolwicz, F. S. Korte, Z. Luo, J. N. Robinson-Hamm, J. L. Page, F. Brozovich, R. S. Weiss, R. Tian, C. E. Murry, and M. Regnier, Proc. Natl. Acad. Sci U.S.A. **110**, 6187 (2013).
[14]S. D. Lundy, S. A. Murphy, S. K. Dupras, J. Dai, C. E. Murry, M. A. Laflamme, and M. Regnier, J. Mol. Cell Cardiol. **72**, 350 (2014).
[15]K. S. Thomson, G. L. Odom, C. E. Murry, G. G. Mahairas, F. Moussavi-Harami, S. L. Teichman, X. Chen, S. D. Hauschka, J. S. Chamberlain, and M. Regnier, JACC: Basic Transl. Sci. **1**, 666 (2016).
[16]S. Kadota, J. Carey, H. Reinecke, J. Leggett, S. Teichman, M. A. Laflamme, C. E. Murry, M. Regnier, and G. G. Mahairas, Eur. J. Heart Fail. **17**, 772 (2015).
[17]S. C. Kolwicz, Jr., G. L. Odom, S. G. Nowakowski, F. Moussavi-Harami, X. Chen, H. Reinecke, S. D. Hauschka, C. E. Murry, G. G. Mahairas, and M. Regnier, Mol. Ther. **24**, 240 (2016).
[18]K. N. Mhatre, J. D. Murray, G. Flint, T. S. McMillen, G. Weber, M. Shakeri, A.-Y. Tu, S. Steczina, R. Weiss, D. J. Marcineck, C. E. Murry, D. Raftery, R. Tian, F. Moussavi-Harami, and M. Regnier, J. Mol. Cell Cardiol. **175**, 1 (2023).
[19]F. S. Korte, J. Dai, K. Buckley, E. R. Feest, N. Adamek, M. A. Geeves, C. E. Murry, and M. Regnier, J. Mol. Cell Cardiol. **51**, 894 (2011).

[20]M. Periasamy and S. Huke, J. Mol. Cell Cardiol. **33**, 1053 (2001).
[21]S. M. Pogwizd, K. Schlotthauer, L. Li, W. Yuan, and D. M. Bers, Circ. Res. **88**, 1159 (2001).
[22]L. Zhihao, N. Jingyu, L. Lan, S. Michael, G. Rui, B. Xiyun, L. Xiaozhi, and F. Guanwei, Heart Fail. Rev. **25**, 523 (2020).
[23]L. J. Motloch, M. Cacheux, K. Ishikawa, C. Xie, J. Hu, J. Aguero, K. M. Fish, R. J. Hajjar, and F. G. Akar, J. Am. Heart Assoc. **7**, e009598 (2018).
[24]C. Hayward, N. R. Banner, A. Morley-Smith, A. R. Lyon, and S. E. Harding, Hum. Gene Ther. **26**, 293 (2015).
[25]T. Tsuji, F. del Monte, Y. Yoshikawa, T. Abe, J. Shimizu, C. Nakajima-Takenaka, S. Taniguchi, R. J. Hajjar, and M. Takaki, Am. J. Physiol. Heart Circ. Physiol. **296**, H310 (2009).
[26]B. Greenberg, J. Butler, G. M. Felker, P. Ponikowski, A. A. Voors, A. S. Desai, D. Barnard, A. Bouchard, B. Jaski, A. R. Lyon, J. M. Pogoda, J. J. Rudy, and K. M. Zsebo, Lancet **387**, 1178 (2016).
[27]Y. Miao, V. A. Feher, and J. A. McCammon, J. Chem. Theory Comput. **11**, 3584 (2015).
[28]J. Wang, P. R. Arantes, A. Bhattarai, R. V. Hsu, S. Pawnikar, Y.-M. M. Huang, G. Palermo, and Y. Miao, Wiley Interdiscip. Rev. Comput. Mol. Sci. **11**, e1521 (2021).
[29]C. Toyoshima, S. Iwasawa, H. Ogawa, A. Hirata, J. Tsueda, and G. Inesi, Nature **495**, 260 (2013).
[30]Y. Kabashima, H. Ogawa, R. Nakajima, and C. Toyoshima, Proc. Natl. Acad. Sci. **117**, 18448 (2020).
[31]G. A. Huber and J. A. McCammon, Comput. Phys. Commun. **181**, 1896 (2010).
[32]Y. Himeno, K. Asakura, C. Y. Cha, H. Memida, T. Powell, A. Amano, and A. Noma, Biophys. J. **109**, 415 (2015).
[33]H. M. Berman, J. Westbrook, Z. Feng, G. Gilliland, T. N. Bhat, H. Weissig, I. N. Shindyalov, and P. E. Bourne, Nucleic Acids Res. **28**, 235 (2000).
[34]T. Schwede, J. Kopp, N. Guex, and M. C. Peitsch, Nucleic Acids Res. **31**, 3381 (2003).
[35]F. Sievers and D. G. Higgins, Protein Sci. **27**, 135 (2018).
[36]J. Lee, D. S. Patel, J. Ståhle, S.-J. Park, N. R. Kern, S. Kim, J. Lee, X. Cheng, M. A. Valvano, O. Holst, Y. A. Knirel, Y. Qi, S. Jo, J. B. Klauda, G. Widmalm, and W. Im, J. Chem. Theory Comput. **15**, 775 (2019).
[37]T. J. Dolinsky, J. E. Nielsen, J. A. McCammon, and N. A. Baker, Nucleic Acids Res. **32**, W665 (2004).
[38]C. R. Søndergaard, M. H. M. Olsson, M. Rostkowski, and J. H. Jensen, J. Chem. Theory Comput. **7**, 2284 (2011).
[39]M. H. M. Olsson, C. R. Søndergaard, M. Rostkowski, and J. H. Jensen, J. Chem. Theory Comput. **7**, 525 (2011).
[40]T. J. Dolinsky, P. Czodrowski, H. Li, J. E. Nielsen, J. H. Jensen, G. Klebe, and N. A. Baker, Nucleic Acids Res. **35**, W522 (2007).
[41]M. A. Lomize, A. L. Lomize, I. D. Pogozheva, and H. I. Mosberg, Bioinformatics **22**, 623 (2006).
[42]R. J. Bick, L. M. Buja, W. B. Van Winkle, and G. E. Taffet, J. Membr. Biol. **164**, 169 (1998).
[43]H. E. Autzen and M. Musgaard, in *P-Type ATPases: Methods and Protocols*, Methods in Molecular Biology, edited by M. Bublitz (Springer, New York, 2016), p. 459.
[44]E. F. Pettersen, T. D. Goddard, C. C. Huang, G. S. Couch, D. M. Greenblatt, E. C. Meng, and T. E. Ferrin, J. Comput. Chem. **25**, 1605 (2004).
[45]X. He, V. H. Man, W. Yang, T.-S. Lee, and J. Wang, J. Chem. Phys. **153**, 114502 (2020).
[46]J. Wang, W. Wang, P. A. Kollman, and D. A. Case, J. Mol. Graph. Model. **25**, 247 (2006).
[47]C. Tian, K. Kasavajhala, K. A. A. Belfon, L. Raguette, H. Huang, A. N. Migues, J. Bickel, Y. Wang, J. Pincay, Q. Wu, and C. Simmerling, J. Chem. Theory Comput. **16**, 528 (2020).
[48]S. Izadi, R. Anandakrishnan, and A. V. Onufriev, J. Phys. Chem. Lett. **5**, 3863 (2014).
[49]S. Miyamoto and P. A. Kollman, J. Comput. Chem. **13**, 952 (1992).
[50]D. A. Case, K. Belfon, I. Y. Ben-Shalom, S. R. Brozell, D. S. Cerutti, T. E. Cheatham III, V. W. D. Cruzeiro, T. A. Darden, R. E. Duke, G. Giambasu, M. K. Gilson, H. Gohlke, A. W. Goetz, R. Harris, S. Izadi, S. A. Izmailov, K. Kasavajhala, A. Kovalenko, R. Krasny, T. Kurtzman, T. S. Lee, S. LeGrand, P. Li, C. Lin, J. Liu, T. Luchko, R. Luo, V. Man, K. M. Merz, Y. Miao, O. Mikhailovskii, G. Monard, H. Nguyen, A. Onufriev, F. Pan, S. Pantano, R. Qi, D. R. Roe, A. Roitberg, C. Sagui, S. Schott-Verdugo, J. Shen, C. L. Simmerling, N. R. Skrynnikov, J. Smith, J. Swails, R. C. Walker, J. Wang, L. Wilson, R. M. Wolf, X. Wu, Y. Xiong, Y. Xue, D. M. York, and P. A. Kollman, *Amber Simulation Software: Citation instructions* (University of California, San Francisco, 2020), https://ambermd.org/CiteAmber.php.
[51]San Diego Supercomputer Center, *Triton Shared Computing Cluster* (University of California, San Diego, 2023).
[52]W. Humphrey, A. Dalke, and K. Schulten, J. Mol. Graph. **14**, 33 (1996).
[53]The PyMOL Molecular Graphics System, Version 2.0 Schrödinger, LLC, 2015.
[54]D. R. Roe and T. E. Cheatham III, J. Chem. Theory Comput. **9**, 3084 (2013).
[55]R. T. McGibbon, K. A. Beauchamp, M. P. Harrigan, C. Klein, J. M. Swails, C. X. Hernández, C. R. Schwantes, L.-P. Wang, T. J. Lane, and V. S. Pande, Biophys. J. **109**, 1528 (2015).
[56]Y. Miao, W. Sinko, L. Pierce, D. Bucher, R. C. Walker, and J. A. McCammon, J. Chem. Theory Comput. **10**, 2677 (2014).
[57]C. Toyoshima, M. Nakasako, H. Nomura, and H. Ogawa, Nature **405**, 647 (2000).
[58]J. Kennedy and R. Eberhart, in *Proceedings of ICNN'95—International Conference on Neural Networks* (IEEE, 1995), Vol. 4, p. 1942.
[59]C. Toyoshima and T. Mizutani, Nature **430**, 529 (2004).
[60]S. Hua, H. Ma, D. Lewis, G. Inesi, and C. Toyoshima, Biochemistry **41**, 2264 (2002).
[61]J. D. Clausen, D. B. McIntosh, B. Vilsen, D. G. Woolley, and J. P. Andersen, J. Biol. Chem. **278**, 20245 (2003).
[62]B. Mueller, M. Zhao, I. V. Negrashov, R. Bennett, and D. D. Thomas, Biochemistry **43**, 12846 (2004).
[63]Y. Huang, H. Li, and Y. Bu, J. Comput. Chem. **30**, 2136 (2009).
[64]G. Inesi, D. Lewis, C. Toyoshima, A. Hirata, and L. Meis, J. Biol. Chem. **283**, 1189 (2008).
[65]G. Inesi, M. Kurzmack, C. Coan, and D. E. Lewis, J. Biol. Chem. **255**, 3025 (1980).
[66]Z. Zhang, D. Lewis, C. Strock, G. Inesi, M. Nakasako, H. Nomura, and C. Toyoshima, Biochemistry **39**, 8758 (2000).
[67]P. M. Kekenes-Huskey, V. T. Metzger, B. J. Grant, and J. A. McCammon, Protein Sci. **21**, 1429 (2012).
[68]A. P. Einholm, B. Vilsen, and J. P. Andersen, J. Biol. Chem. **279**, 15888 (2004).
[69]A. G. Lee and J. M. East, Biochem. J. **356**, 665 (2001).
[70]M. Musgaard, L. Thøgersen, B. Schiøtt, and E. Tajkhorshidk, Biophys. J. **102**, 268 (2012).